Optimization of ruthenium as a buffer layer for non-collinear antiferromagnetic Mn_3X films

S. Kurdi[1,*], P. Zilske[2], X.D. Xu[3,†], M. Frentrup[1], M.E. Vickers[1], Y. Sakuraba[3], G. Reiss[2], Z.H. Barber[1] and J.W. Koo[2,‡]

[1] Department of Materials Science and Metallurgy, University of Cambridge, CB3 0FS Cambridge, United Kingdom.

[2] Center for Spinelectronic Materials and Devices, Bielefeld University, D-33501 Bielefeld, Germany

[3] National Institute for Materials Science (NIMS), 1-2-1 Sengen, Tsukuba 305-0047, Japan

[†] Present address: College of Materials Science and Engineering, Hunan University, Changsha 410082, China

* sk862@cam.ac.uk

‡ jkoo@physik.uni-bielefeld.de

Abstract

Two thin film deposition routes were studied for the growth of high quality single crystalline Ru (0001) epitaxial films on *c*-Al_2O_3 substrates using RF-magnetron sputtering. Such films are very important as buffer layers for the deposition of epitaxial non-collinear antiferromagnetic Mn_3X films. The first route involved depositing Ru at 700 °C, leading to a smooth 30 nm thick film. Although, high resolution X-ray diffraction (HRXRD) revealed twinned Ru film orientations, the *in-situ* post-annealing eliminated one orientation, leaving the film orientation aligned with the substrate, with no in-plane lattice rotation and a large lattice mismatch (13.6%). The second route involved deposition of Ru at room temperature followed by *in-situ* post-annealing at 700 °C. Transmission electron microscopy confirmed a very high quality of these films, free of crystal twinning, and a 30° in-plane lattice rotation relative to the substrate, resulting in a small in-plane lattice mismatch of –1.6%. X-ray reflectivity demonstrated smooth surfaces for films down to 7 nm thickness. 30 nm thick high quality single-crystalline Mn_3Ga and Mn_3Sn films were grown on top of the Ru buffer deposited using the second route as a first step to realize Mn_3X films for antiferromagnetic spintronics applications.

Introduction

In the past decade, antiferromagnets have come to the forefront for spin-electronics (spintronics) research. Utilizing antiferromagnets as a main component for spintronic devices allows for the realization of denser and more robust data storage capabilities compared to ferromagnetic devices due to the intrinsic properties of antiferromagnetic order[1]. However, in general, the manipulation of their magnetic order requires very large magnetic fields limiting their implementation. Antiferromagnetic systems, like non-collinear ε-Mn_3X (X = Sn, Ge, Ga), have shown properties that promise to overcome this bottleneck. Their topologically non-trivial band structure exhibiting Weyl nodes[2] and their geometrical frustrated spin structure leads to the anomalous Hall[3] and Nernst[4] effects in addition to the magneto-optical Kerr effect[5] which are forbidden in usual antiferromagnets. This is of great importance as it could lead to future spintronic devices in which antiferromagnets play the major role. Many of the recent studies have been on bulk Mn_3X {X = Sn, Ge)[3,6], whilst thin film investigations have focused on polycrystalline or textured films for exchange bias applications[7–10]. However, epitaxial Mn_3Sn films deposited on Ru (5 nm) buffered Y:ZrO_2 substrates were not continuous due to island formation[9], making it not possible to measure their transport properties. In other reports quasi-epitaxial Mn_3Sn $(11\bar{2}0)$ and (0001)-oriented thin films deposited on Al_2O_3 $(1\bar{1}02)$ and MgO (111) substrates, respectively[11], and epitaxial Mn_3Sn films grown on Ru (5 nm) buffered MgO (111)[12] showed dissimilar magnetization properties to those of bulk samples, implying that there is scope for improvement in preparation of these films.

In order to exploit the properties of Mn_3X for device applications, high quality epitaxial thin films are required. Although, Mn_3X films can be grown on a single crystalline substrate sharing the same crystal structure, e.g., c-plane sapphire (c-Al_2O_3), a large lattice mismatch between Mn_3X films and the c-Al_2O_3 substrate hinders the smooth epitaxial growth of Mn_3X thin films. This constraint can be removed if one utilizes an appropriate buffer layer to minimize the lattice mismatch. In this work, we study hexagonal Ru as a buffer layer for Mn_3X films. Ru has very good lattice matching with Mn_3X in the a-plane: ~0.2%, 1.3%, 4.5% misfit for Mn_3Ga, Mn_3Ge and Mn_3Sn respectively, suggesting that a highly epitaxial Ru buffer layer on c-Al_2O_3 will promote smooth epitaxial growth of Mn_3X films. In addition to the close lattice match, Al_2O_3 substrates are very stable, with no requirement for specific surface preparations. In contrast, MgO substrates require annealing to remove surface contamination[13] and are known to lack consistency in quality[14,15].

We demonstrate that a Ru buffer layer on *c*-Al_2O_3 can effectively support the subsequent growth of highly epitaxial Mn_3X thin films. Although the growth of Ru on *c*-Al_2O_3[16–20] has been reported and various techniques have been used to deposit thin Ru films, including pulsed laser deposition (PLD)[18,19,21], e-beam evaporation[22], metal-organic chemical vapour deposition (MOCVD)[23,24], and atomic layer deposition (ALD)[25], there is some discrepancy between studies of the resultant crystalline orientation. In this work, we utilize RF magnetron sputtering[17,20,26,27] to devise a thin film deposition procedure for high quality Ru thin films and demonstrate that a single-crystalline epitaxial Ru thin film is suitable for the subsequent growth of highly epitaxial Mn_3X thin films.

Experimental Methods

Ru thin films were deposited onto *c*-Al_2O_3 substrates using RF-magnetron sputter deposition from a 2-inch diameter Ru target (99.95% purity), in a UHV sputtering chamber built by BESTEC GmbH (Berlin), with a base pressure below 1 x 10^{-8} Pa. The substrates were loaded directly from the supplier's (CrysTec GmbH) vacuum-sealed packaging, with no further surface preparation. Film deposition took place at an Ar (6N) gas pressure of 0.2 Pa. The substrates (10 x 10 mm^2) were rotated at 10 RPM to ensure uniform deposition across the surface. A radiative heater, positioned at the back of the sample holder, allowed control of the growth temperature.

Two routes were followed for Ru thin film growth:
(i) deposition at a relatively high substrate temperature, T_s = 700 °C, followed by *in situ* post-annealing (in vacuum) at the same temperature, and
(ii) deposition at room temperature, followed by *in situ* post-annealing (in vacuum) at T_s = 700 °C (heating rate = 15 °C min^{-1})

Further samples were grown via route (ii), followed by the deposition of 30 nm Mn_3Ga (Mn_3Sn) films at 600 °C (350 °C) on top of the 7 nm thick Ru-buffer via DC-magnetron co-sputter deposition using 2-inch Mn:Ga (50:50 at%, 99.97% purity) / Mn:Sn (65:35 at%, 99.9% purity) and an additional Mn target (99.9% purity)**.** The Mn_3Ga (Mn_3Sn) films were capped with a 2 nm Ru layer at room temperature. The deposition rates of ~1.8 Å s^{-1} (Ru), ~1.3 Å s^{-1} (Mn_3Ga) and ~1.1 Å s^{-1} (Mn_3Sn), were first calibrated *in situ*, using a quartz crystal microbalance, and confirmed by X-ray Reflectivity (XRR) measurement. The actual compositions of the films were $Mn_{72\pm3}Ga_{28\pm1}$ and $Mn_{75\pm1}Sn_{25\pm4}$, as determined by X-ray

fluorescence (XRF), which are within the stable compositional range of the $D0_{19}$ phase of Mn_3Ga[28] and Mn_3Sn[29].

High-resolution X-ray Diffraction (HRXRD) was performed using a four-circle Panalytical Empyrean vertical θ/θ diffractometer with a hybrid 2-bounce primary monochromator. A proportional counter was used for the $2\theta/\theta$ and φ scans and a 2D PIXCEL position sensitive detector (PSD) for collecting the reciprocal space maps (RSMs). A Philips X'Pert Pro MPD θ/θ diffractometer was used to obtain the XRR scans. Cross-sectional lamellae were produced using focused ion-beam (FEI Helios G4 UX) lift-out technique. The cross section of a 7 nm thick Ru film prepared via route (ii) was investigated using a FEI Titan G2 80-200 scanning/transmission electron microscope (S/TEM) with probe corrector operated at 200 kV. The images were taken in both annular dark field (ADF) and high angle annular dark field (HAADF) modes. A condenser aperture of 10 μm was used to collect the selected area electron diffraction (SAED) patterns.

Results and Discussion

Route (i): Fig. 1 shows XRD and XRR results for three Ru films of nominal 5 nm, 15 nm and 30 nm, grown at T_s = 700 ºC, with a subsequent 20 minute, 700 ºC anneal. Fig.1(a) shows XRD $2\theta/\theta$ scans around the (0002) and (0004) Ru reflections, revealing that no other phases, nor orientations, are present. The film peaks are also observed in the same position implying a constant out-of-plane lattice parameter for all three thicknesses. Clear satellite peaks (thickness fringes), illustrating very uniform film growth, are observed for the 30 nm thick film, but are much less prominent for the thinner films. These observations are supported by the XRR scans in Fig.1(b), revealing sharp Kiessig fringes over the entire 5° range for the 30 nm thick film, in which the roughness is determined to be ~5.8 Å from the scan simulation. However, the Kiessig fringes are relatively weak for the thinner films, indicating that they have a rougher surface, as observed by atomic force microscopy (AFM) (Supplementary Note 1). This is consistent with the shift of the critical edge towards lower angles, indicating a lower average density close to the Ru surface compared to thick well crystalline Ru films. Although the oscillations in the XRR signal are relatively weak for the thinner films, which makes a simulation and fit of the signal difficult, the periodicity of the oscillations of the scans suggest thicknesses of ~21 nm and ~10 nm (expected to be 15 nm and 5 nm respectively from the sputtering rates, assuming a uniform thickness). These observations correspond with the vertical coherence length calculation using Scherrer's formula[30] (Supplementary Note 2).

φ-scans from the Ru $(10\bar{1}1)$ and Al_2O_3 $(11\bar{2}3)$ reflections of the 30 nm film are shown in Fig.2(a), giving information about the in-plane film orientation. The lattice constants for Ru and Al_2O_3 are a_{Ru} = 2.706 Å (c = 4.281 Å)[31] and $a_{Al_2O_3}$ = 4.763 Å ($c_{Al_2O_3}$ = 12.991 Å), respectively. Therefore, the in-plane lattice misfit for *c*-plane Ru growth, if the axes line up, is 13.6%. However, a 30° in-plane rotation of the Ru film lattice relative to *c*-Al_2O_3 leads to an in-plane lattice mismatch of only –1.6%, since $a_{Al_2O_3} \sim 2a_{Ru}\cos 30°$. This low lattice misfit configuration, with a 30° in-plane lattice rotation, would lead to 6-fold symmetry with Ru $(10\bar{1}1)$ peaks coincident with the Al_2O_3 $(11\bar{2}3)$ reflections. However, the 6 broad grey peaks of Fig. 2(a) (marked with grey arrows) indicate an unrotated lattice. The narrower (and less intense) reflections between these peaks could be 30º-rotated Ru. However, since the Al_2O_3 $(11\bar{2}3)$ and Ru $(10\bar{1}1)$ reflections have very similar diffraction conditions (for Ru $(10\bar{1}1)$, 2θ = 43.960°, χ = 61.27°; and for Al_2O_3 $(11\bar{2}3)$, 2θ = 43.352°, χ = 61.21°), these intermediate reflections could be trace signals from the very strong Al_2O_3 $(11\bar{2}3)$ peaks. This is mirrored in the Al_2O_3 $(11\bar{2}3)$ φ-scan (bottom of Fig.2(a)), for which the narrow, intense peaks stem from the single crystal substrate, and the less intense intermediate peaks are traces of the Ru $(10\bar{1}1)$ reflections.

To gain further information on the in-plane orientation of this Ru film, χ was set at 61.20° and $2\theta/\theta$ scans were taken at φ = 0° and φ = 30° (Fig. 2(b)). The Al_2O_3 peak only appears at φ = 0º, whilst a Ru peak appears at both angles, indicating the presence of two, twin-related[32] film orientations, and confirming that all 12 peaks in the top trace of Fig. 2(a) correspond to Ru reflections. Such twinning has been observed for other Pt-group metals deposited on sapphire as well.[22] Here, the Ru with crystalline axes aligned with the sapphire shows a relatively higher intensity than the 30° in-plane rotated lattice, indicating that the majority of the Ru film has lined axes with the Al_2O_3 substrate. For reference, see Fig. 2(c)) for a schematic of the Ru lattice aligned with the sapphire and 30° in-plane rotated relative to the sapphire lattice.

To investigate the influence of annealing duration on the quality of Ru thin film, 30 nm Ru films were deposited at T_s = 700 ºC, followed by *in situ* 700 ºC anneals of varying times. Fig. 3 shows RSMs of the Ru $(10\bar{1}3)$ reflection at φ = 0° and 30º, acquired for post-anneals of 20, 30 and 60 minutes. In the φ = 0° case, the RSM was obtained by simply aligning to the nearby Al_2O_3 $(11\bar{2}9)$ reflection. However, since rotating φ by 30º removes this Al_2O_3 reflection, an accurate Ru $(10\bar{1}3)$ position was achieved in this case by alignment on the Al_2O_3 $(10\bar{1}\,10)$ reflection, and subsequently adjusting 2θ and ω. Fig. 3 illustrates the two, twinned Ru orientations: with the lattice aligned with the sapphire lattice (bottom, higher intensity), and

30° rotated to each other (top). Increase of annealing time leads to severe reduction of one of these orientations (Fig. 3(b) and (c)): following a 60 minute post-anneal, the twinning is virtually eliminated, leaving only the film orientation aligned with the substrate, with no in-plane lattice rotation: Ru (0001)$[10\bar{1}0]$ || Al_2O_3 (0001)$[10\bar{1}0]$. Whilst inconsistent with the lowest lattice mismatch (–1.6%) relationship discussed above: Ru (0001)$[10\bar{1}0]$ || Al_2O_3 (0001)$[11\bar{2}0]$[19,20], this film orientation has also been reported by Sutter *et al.*[16] for films deposited by RF sputtering at T_s = 650 °C, and post-annealed at 850 °C for 15 minutes. Such epitaxial relationship has been attributed to the accommodation of the large epitaxial mismatch (13.6%) to relaxation of the film lattice through a network of interfacial dislocations[19,20].

The out-of-plane lattice constants of our Ru films were calculated from the (0002) and (0004) XRD peak positions, and the in-plane lattice constants from the $(10\bar{1}3)$ and $(10\bar{1}4)$ peaks. The lattice parameters are comparable to the bulk values (a = 2.706 Å, c = 4.281 Å)[31], see Table 2, indicating complete strain relaxation. The out of plane lattice parameter (c) is within 0.03% of the bulk and the in-plane within 0.07% of the bulk value.

Whilst we have demonstrated that growth at 700 °C, followed by a 60 minute 700 °C anneal, can lead to very high quality, single-orientation Ru films, with bulk lattice parameters, films thinner than 30 nm proved to be of lower quality, due to a higher surface roughness – see Fig. 1(b). For future antiferromagnetic Mn_3X spintronic devices, a thick Ru buffer layer hinders the measurement of phenomenon like the anomalous Hall and spin Hall effects, since most of the electric current will flow through the thick Ru buffer layer due to its high conductivity. Therefore we sought to find a different deposition process to realize thinner Ru films that maintain a comparable crystalline quality as the 30 nm film prepared by route (i).

Route (ii): $2\theta/\theta$ XRD scans of 7 nm, 15 nm and 30 nm thick Ru films, deposited by RF-magnetron sputtering at room temperature and *in situ* post-annealed at 700 °C for 60 minutes, are shown in Fig. 4(a). In contrast with Fig. 1(a), all XRD scans show thickness fringes. XRR scans (Fig. 4(b)) exhibit clear Kiessig fringes, indicating smooth interfaces and confirming that high quality film growth was achieved for all thicknesses. The estimated values for roughness obtained from the simulated XRR data for the 30 nm, 15 nm and 7 nm are 3.3 Å, 2.5 Å and 2.7 Å respectively. Fig. 4(c) shows φ-scans from the Ru $(10\bar{1}1)$ and Al_2O_3 $(11\bar{2}3)$ reflections of the 30 nm film, illustrating the in-plane film orientation. In this case 6-fold symmetry is observed in the Ru film, with the film and substrate peaks aligned, suggesting the lower lattice misfit Ru (0001)$[10\bar{1}0]$ || Al_2O_3 (0001)$[11\bar{2}0]$ epitaxial relationship (i.e. the Ru lattice is 30°

rotated in-plane relative to *c*-Al_2O_3). This orientation has also been reported by Brandenburg et al.[19] (using PLD) and Milosevic et al.[20] (DC-magnetron sputtering), with film growth at a low T_s and a subsequent higher temperature *in situ* annealing.

RSMs of the Ru $(10\bar{1}3)$ reflection at $\varphi = 0°$ and 30º (Supplementary Note 3) for a 30 nm thick film support the results of Fig. 4.: no Ru $(10\bar{1}3)$ reflection is observed at $\varphi = 30°$, confirming the Ru $(0001)[10\bar{1}0]$ || Al_2O_3 $(0001)[11\bar{2}0]$ epitaxial relationship. The lattice constants were determined from the $2\theta/\theta$ XRD scans (Fig. 4 (a)) and RSM (Supplementary Note 4). The lattice parameters, given in Table 2, are comparable to the bulk values, indicating that the films are relaxed, even at 7 nm. The out of plane lattice constant (*c*) is within ~0.02% of the bulk and the in-plane (*a*) varies within ~0.04 – 0.18% of the bulk value.

The structure and orientation of a 7 nm thick Ru film, deposited at room temperature and post-annealed for 60 minutes *in situ* at 700 °C, was investigated by high resolution S/TEM (Fig. 5). Fig. 5(a) shows the Ru film on top of the *c*-Al_2O_3 substrate. The film was observed to have a uniform thickness (confirmed over a 1.5 µm length scale) and low interfacial roughness, with Ru (0001) lattice planes observed to be parallel to the substrate surface. The image also shows a very smooth Al_2O_3/Ru interface with only three, monolayer high steps across a range of 13 nm width. The inset in Fig. 5(a) shows an enlarged area, confirming very high crystalline film quality. SAED patterns, with the electron beam parallel to the *c*-Al_2O_3 $[11\bar{2}0]$ zone axis, reveal that the $[10\bar{1}0]$ Ru-axis (Fig. 5(b)) is parallel to the $[11\bar{2}0]$ axis of Al_2O_3 (Fig. 5(c)), confirming the epitaxial relationship inferred from the XRD data.

The results from route (i) imply that the higher deposition temperature promotes mobility of Ru adatoms and clusters on the substrate surface during film growth, leading to island-growth. As the film thickens, individual islands coalesce into larger grains, and twin boundaries form between islands that have nucleated in the two different symmetry-related orientations: high misfit (aligned with the substrate crystal axes), and low misfit (with a 30° rotation). Fig. 2(b) illustrates that the higher misfit (13.6%) orientation is dominant with a more intense Ru $(10\bar{1}1)$ reflection. A longer post-deposition anneal promotes domain growth (loss of twin boundaries), with this dominant orientation increasing and, after 60 minutes, this single film orientation remains. It appears that the high lattice mismatch is accommodated through relaxation during annealing, leaving a network of interfacial dislocations[16]. In contrast, deposition at room temperature (route (ii)) is likely to take place through layer-by-layer growth, leading to the lower misfit (30º rotated) crystalline orientation, smaller grain sizes (see calculated lateral coherence lengths in Supplementary Note 2) and smooth surfaces for all film thicknesses.

Finally, 30 nm thick Mn_3Ga and Mn_3Sn films were then deposited on an optimized 7 nm Ru buffer layer (route (ii)) to verify if epitaxial and homogenous Mn_3X films can be achieved. Fig. 6 summarizes the Mn_3Ga and Mn_3Sn structural characterization using XRD. Fig.6(a) and (b) shows XRD $2\theta/\theta$ scans around the (0002) Mn_3Ga and Mn_3Sn peaks respectively (no other phases, nor orientations, were observed), indicating that highly epitaxial growth of the films on an optimized Ru buffer layer has been achieved. Both films are relaxed as the Mn_3X reflection do not align in S_x with the Al_2O_3 $(11\bar{2}9)$ reflections as indicated by the RSMs, in Fig. 6(c) and (d) for Mn_3Ga and Mn_3Sn respectively. The epitaxial relationship as implied by Fig. 6(c) and (d) for Mn_3Ga and Mn_3Sn and as supported by φ –scans (Supplementary Note 5) is: Mn_3X (X = Ga, Sn) $(0001)[20\bar{2}0]$ || Ru $(0001)[10\bar{1}0]$ || Al_2O_3 $(0001)[11\bar{2}0]$. The highly epitaxial and single-phase Mn_3Ga and Mn_3Sn thin films deposited on the on the optimized thin Ru buffer layer have bulk-like lattice constants (Table 3) and are therefore promising to investigate the intriguing spintronic effects originating from the non-collinear antiferromagnetic order of these systems.

In summary, we have presented two deposition routes for Ru thin films on c-Al_2O_3 substrates. Depositing the films at 700 °C resulted in twinned Ru orientations and rough surfaces when the nominal film thickness was ≤ 15 nm. Subsequent in-situ post annealing at 700 °C led to a single in-plane orientation of Ru (Ru 0° rotated relative to the c-Al_2O_3 substrate), however did not improve the surface morphology. Depositing at room temperature followed by in-situ post-annealing at 700 °C resulted in the higher quality films down to 7 nm with no twinned grains. In addition, we also showed that highly epitaxial and single phase Mn_3X (X = Ga, Sn) on top of the optimized Ru film can be grown with a Mn_3X (X = Ga, Sn) $(0001)[20\bar{2}0]$ || Ru $(0001)[10\bar{1}0]$ || Al_2O_3 $(0001)[11\bar{2}0]$ epitaxial relationship, that promises bulk-like magnetic and transport properties, which will be investigated in future studies.

Supplementary

See supplementary material for the following notes:

Note 1: Atomic Force Microscopy
Note 2: Vertical and lateral coherence length for the Ru and the Mn_3X films.
Note 3: RSM of the Ru $(10\bar{1}3)$ reflection for a 30 nm thick Ru film taken at φ = 0° and 30°.
Note 4: RSM of the Ru $(10\bar{1}3)$ reflection for 30 nm, 15 nm, and 7 nm thick Ru films.
Note 5: φ-scans of the Mn_3X (X = Ga, Sn) $(20\bar{2}1)$, Ru $(10\bar{1}1)$ and Al_2O_3 $(11\bar{2}3)$ reflections.

Acknowledgements

This work was funded by the H2020-MSCA-ITN-2014 SELECTA (grant agreement no. 642642 of the European Commission).

Tables

Table 1. The lattice constants for 30 nm thick Ru films deposited at 700 °C and post-annealed *in situ* for 20, 30 and 60 minutes.

	***c* (Å)**	***a* (Å)**	
Post Anneal Time (min)		**φ = 0°**	**φ = 30°**
20	4.282 ± 0.001	2.707 ± 0.002	2.706 ± 0.001
30	4.282 ± 0.001	2.708 ± 0.002	2.707 ± 0.001
60	4.282 ± 0.001	2.708 ± 0.001	2.707 ± 0.001

Table 2. Lattice constants for 7 nm, 15 nm, and 30 nm Ru films deposited at room temperature and post-annealed *in situ* at 700 °C for 60 minutes.

Thickness (nm)	***c* (Å)**	***a* (Å)**
7	4.282 ± 0.001	2.711 ± 0.002
15	4.281 ± 0.001	2.707 ± 0.001
30	4.280 ± 0.001	2.708 ± 0.001

Table 3. Lattice constants for 30 nm Mn_3Ga and Mn_3Sn films deposited on a 7 nm Ru buffer (route (ii)).

Films	***c* (Å)**	***a* (Å)**
Mn_3Ga	4.353 ± 0.002	5.433 ± 0.002
Mn_3Sn	4.530 ± 0.001	5.670 ± 0.002

Figures

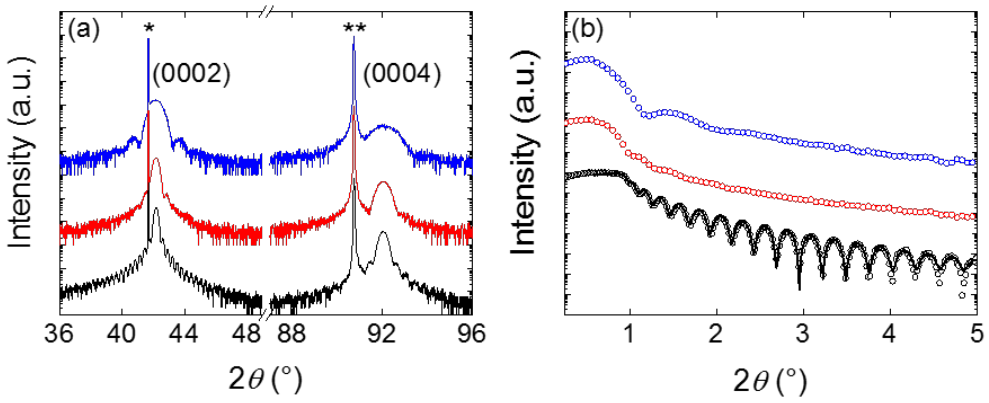

Figure 1. (a) $2\theta/\theta$ XRD, and (b) XRR scans for 30 nm (black), 15 nm (red) and 5 nm (blue) Ru films deposited at 700 °C and post-annealed *in situ* for 20 minutes at the same temperature. * and ** indicate the Al_2O_3 (0006) and (000 12) reflections respectively. The open circles and the solid lines represent the measured and simulated curves respectively.

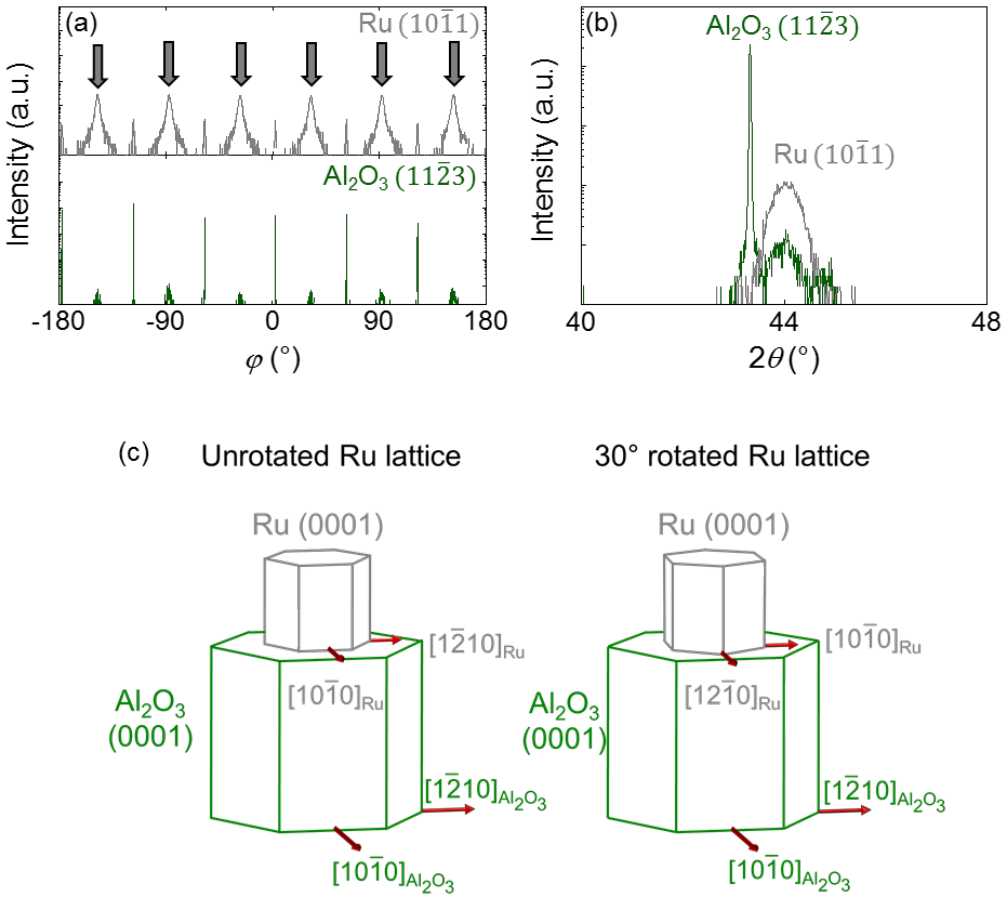

Figure 2. (a) Al_2O_3 (11$\bar{2}$3) (green) and Ru (10$\bar{1}$1) (grey) φ-scans for a 30 nm thick Ru film sample deposited at 700 °C and post-annealed (20 minutes) at the same temperature. (b) $2\theta/\theta$ XRD scans at $\chi = 61.20°$ with $\varphi = 0°$ (green) and $\varphi = 30°$ (grey). (c) Schematic of an Ru lattice aligned with the sapphire lattice (left) and 30° rotated about the sapphire lattice.

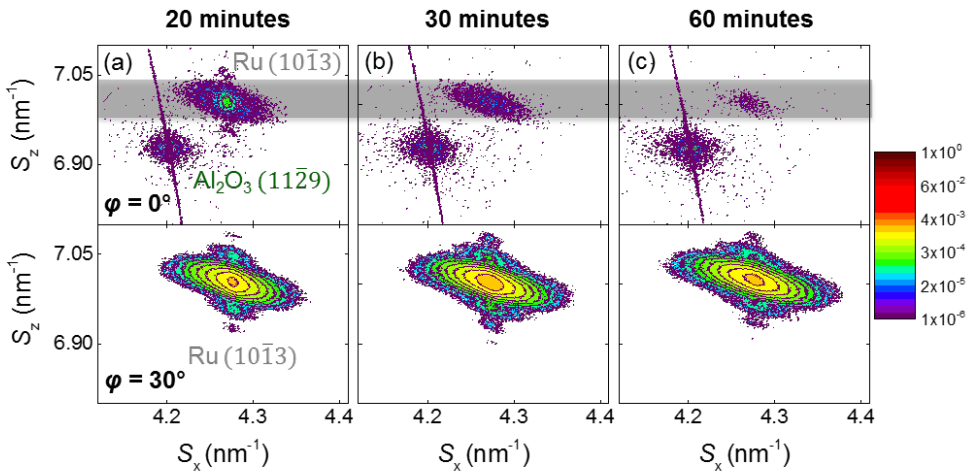

Figure 3. Ru (10$\bar{1}$3) RSMs at $\varphi = 0°$ and $\varphi = 30°$ for 30 nm thick Ru films deposited at 700 °C and post-annealed for 20 minutes (a), 30 minutes (b) and 60 minutes (c). The grey shading represents the position of the Ru (10$\bar{1}$3) reflection in the case of a 30°-rotated Ru lattice relative to Al_2O_3.

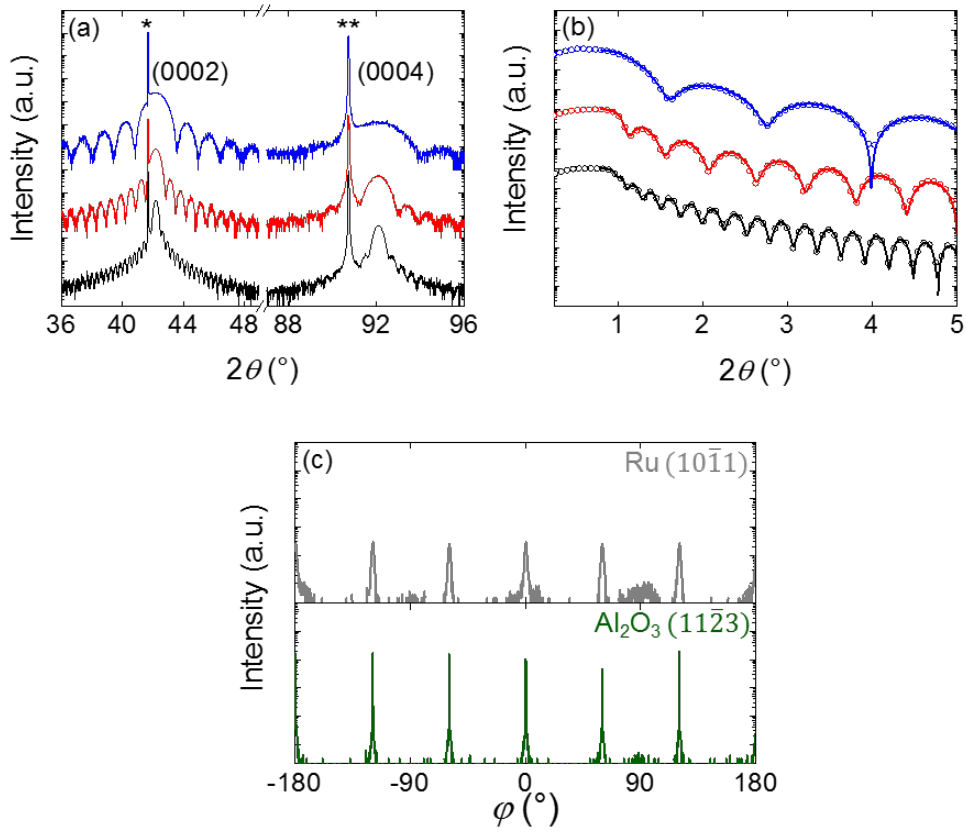

Figure 4. (a) $2\theta/\theta$ XRD scans and (b) XRR scans for 30 nm (black), 15 nm (red), and 7 nm (blue) Ru films deposited at room temperature and post-annealed *in situ* at 700 °C for 60 minutes. The open circles and the solid lines represent the measured and simulated curves respectively. (c) Al_2O_3 (11$\bar{2}$3) (green) and Ru (10$\bar{1}$1) (grey) φ-scans for a 30 nm thick Ru film deposited at room temperature and post-annealed *in situ* for 60 minutes at 700 °C. * and ** indicate the Al_2O_3 (0006) and (000 12) reflections respectively.

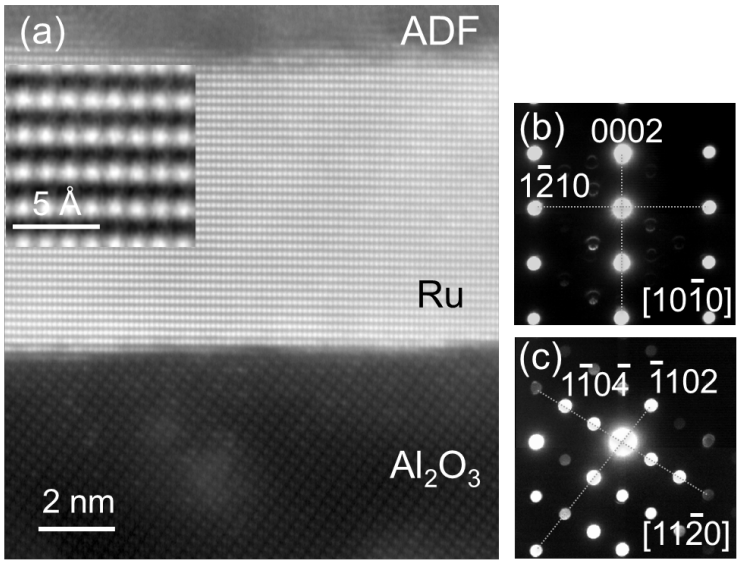

Figure 5. (a) A STEM cross-sectional image of a 7 nm thick Ru film deposited on *c*-Al_2O_3 via route (ii). The inset shows a HAADF-STEM image of enlarged area of the Ru film. (b) SAED patterns obtained along the [11$\bar{2}$0] zone axis of Al_2O_3 for the (b) Ru and (c) Al_2O_3 layers. The dashed grey lines are guides for the eye only.

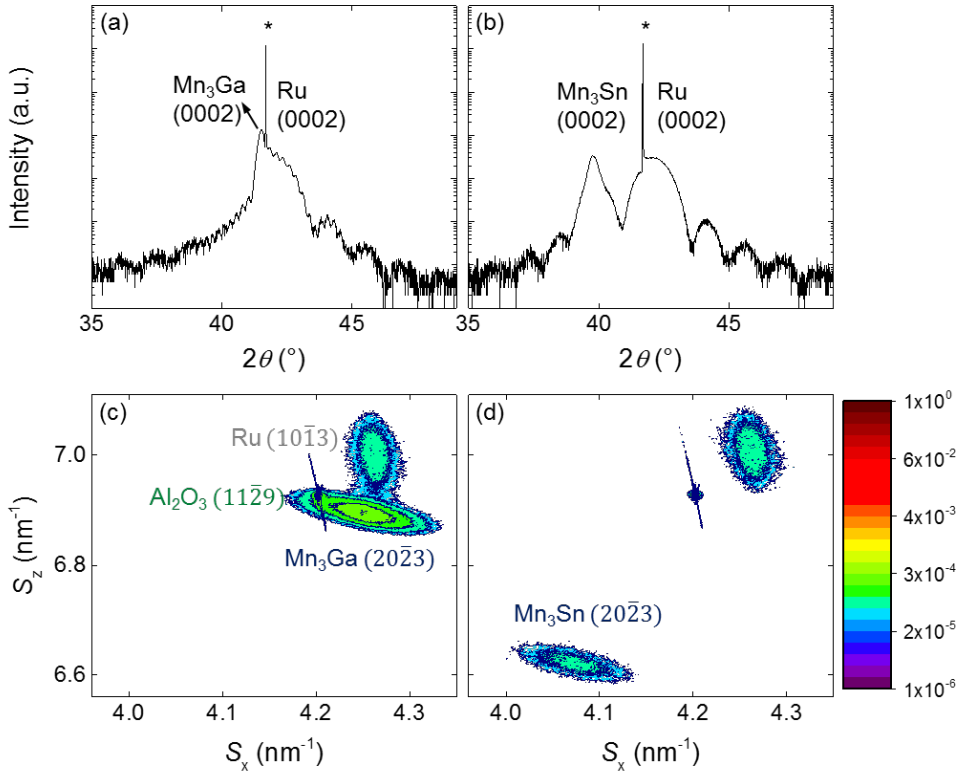

Figure 6. 2θ/θ XRD scans for 30 nm thick (a) Mn_3Ga and (b) Mn_3Sn deposited on a 7 nm thick Ru film deposited at 700 °C and post-annealed *in situ* for 20 minutes at the same temperature. RSM for the same Mn_3Ga and (d) Mn_3Sn films focusing on the (20$\bar{2}$3) reflection. * Indicates the Al_2O_3 (0006) reflection.

References

[1] T. Jungwirth, X. Marti, P. Wadley, and J. Wunderlich, Nat. Nanotechnol. **11**, 231 (2016).

[2] K. Kuroda, T. Tomita, M.-T. Suzuki, C. Bareille, A.A. Nugroho, P. Goswami, M. Ochi, M. Ikhlas, M. Nakayama, S. Akebi, R. Noguchi, R. Ishii, N. Inami, K. Ono, H. Kumigashira, A. Varykhalov, T. Muro, T. Koretsune, R. Arita, S. Shin, T. Kondo, and S. Nakatsuji, Nat. Mater. **16**, 1090 (2017).

[3] S. Nakatsuji, N. Kiyohara, and T. Higo, Nature **527**, 212 (2015).

[4] M. Ikhlas, T. Tomita, T. Koretsune, M.T. Suzuki, D. Nishio-Hamane, R. Arita, Y. Otani, and S. Nakatsuji, Nat. Phys. **13**, 1085 (2017).

[5] T. Higo, H. Man, D.B. Gopman, L. Wu, T. Koretsune, O.M.J. Van 'T Erve, Y.P. Kabanov, D. Rees, Y. Li, M.T. Suzuki, S. Patankar, M. Ikhlas, C.L. Chien, R. Arita, R.D. Shull, J. Orenstein, and S. Nakatsuji, Nat. Photonics **12**, 73 (2018).

[6] A.K. Nayak, J.E. Fischer, Y. Sun, B. Yan, J. Karel, A.C. Komarek, C. Shekhar, N. Kumar, W. Schnelle, J. Kübler, C. Felser, and S.S.P. Parkin, Sci. Adv. **2**, e1501870 (2016).

[7] H. Kurt, K. Rode, M. Venkatesan, P. Stamenov, and J.M.D. Coey, Phys. Status Solidi Basic Res. **248**, 2338 (2011).

[8] H. Wu, I. Sudoh, R. Xu, W. Si, C.A.F. Vaz, J.Y. Kim, G. Vallejo-Fernandez, and A. Hirohata, J. Phys. D. Appl. Phys. **51**, 215003 (2018).

[9] A. Markou, J.M. Taylor, A. Kalache, P. Werner, S.S.P. Parkin, and C. Felser, Phys. Rev. Mater. **2**, 051001 (2018).

[10] T. Ogasawara, J. Kim, Y. Ando, and A. Hirohata, J. Magn. Magn. Mater. **473**, 7 (2019).

[11] Y. You, X. Chen, X. Zhou, Y. Gu, R. Zhang, F. Pan, and C. Song, Adv. Electron. Mater. **5**, 1800818 (2019).

[12] H. Reichlova, T. Janda, J. Godinho, A. Markou, D. Kriegner, R. Schlitz, J. Zelezny, Z. Soban, M. Bejarano, H. Schultheiss, P. Nemec, T. Jungwirth, C. Felser, J. Wunderlich, and S.T.B. Goennenwein, Nat. Commun. **10**, 5459 (2019).

[13] W. Hsu, H. Kao, and Z. Lin, J. Cryst. Growth **436**, 46 (2016).

[14] J.L. Schroeder, A.S. Ingason, J. Rosén, and J. Birch, J. Cryst. Growth **420**, 22 (2015).

[15] R. Suzuki, A. Kawaharazuka, and Y. Horikoshi, J. Cryst. Growth **311**, 2021 (2009).

[16] P.W. Sutter, P.M. Albrecht, and E.A. Sutter, Appl. Phys. Lett. **97**, 213101 (2010).

[17] S. Yoshii, K. Nozawa, K. Toyoda, N. Matsukawa, A. Odagawa, and A. Tsujimura, Nano Lett. **11**, 2628 (2011).

[18] S. Yamada, Y. Nishibe, M. Saizaki, H. Kitajima, S. Ohtsubo, A. Morimoto, T. Shimizu, K. Ishida, and Y. Masaki, Jpn. J. Appl. Phys. **41**, L206 (2002).

[19] J. Brandenburg, R. Hühne, L. Schultz, and V. Neu, Phys. Rev. B **79**, 054429 (2009).

[20] E. Milosevic, S. Kerdsongpanya, A. Zangiabadi, K. Barmak, K.R. Coffey, and D. Gall, J. Appl. Phys. **124**, 165105 (2018).

[21] T. Kim, T. Kawae, N. Ikegami, S. Yamada, Y. Yonezawa, K. Takahashi, A. Morimoto, and M. Kumeda, Jpn. J. Appl. Phys. **47**, 6374 (2008).

[22] S. Gsell, M. Fischer, M. Schreck, and B. Stritzker, J. Cryst. Growth **311**, 3731 (2009).

[23] T. Shibutami, K. Kawano, N. Oshima, S. Yokoyama, and H. Funakubo, Electrochem. Solid-State Lett. **6**, C117 (2003).

[24] K. Kawano, A. Nagai, H. Kosuge, T. Shibutami, N. Oshima, and H. Funakubo, Electrochem. Solid-State Lett. **9**, C107 (2006).

[25] M. Change, S. Ganguli, and N. Maity, US 7,264,846 B2 (2007).

[26] T.N. Arunagiri, Y. Zhang, O. Chyan, M. El-Bouanani, M.J. Kim, K.H. Chen, C.T. Wu, and L.C. Chen, Appl. Phys. Lett. **86**, 083104 (2005).

[27] S.H. Park, S.O. Kim, T.D. Lee, H.S. Oh, Y.S. Kim, N.Y. Park, and D.H. Hong, J. Appl. Phys. **99**, 08E701 (2006).

[28] E. Krén and G. Kádár, Solid State Commun. **8**, 1653 (1970).

[29] E. Krén, J. Paitz, G. Zimmer, and E. Zsoldos, Physica **80B**, 226 (1975).

[30] P. Scherrer, Nachr Ges Wiss Göttingen **26**, 387 (1912).

[31] M. Černohorský, Acta Crystallogr. **13**, 823 (1960).

[32] B.D. Cullity and S.R. Stock, *Elements of X-Ray Diffraction*, 3rd ed. (Pearson Education Limited, London, UK, 2014).